Welding of Nickel-Based Alloys for Energy Applications

*A summary of the Comfort A. Adams Lecture presented at
the 2013 AWS Annual Meeting*

BY JOHN N. DuPONT

ABSTRACT

The development of new engineering alloys with improved strength and corrosion resistance is vital to the production of energy from a wide variety of sources. In many applications, critical components used in energy production will require welding during initial fabrication, maintenance, and repair. Nickel-based alloys are expected to play a key role in this area since they can often provide levels of high-temperature strength and corrosion resistance that cannot be obtained with ferritic steels or austenitic alloys. However, the thermal cycle associated with welding causes significant microstructural modification to these alloys, usually in a manner that has a detrimental impact on properties. Thus, it is important to understand and control these modifications so that full-scale use of new Ni-based alloys is not limited when welding is required as a means of construction. This article summarizes some recent advances made at Lehigh University in the last ~ 10 years toward understanding the welding metallurgy and weldability of Ni-based alloys for energy applications. The use of new computational tools and microstructural characterization techniques have been important for obtaining a detailed understanding of welding metallurgy issues, and examples are provided in this review. The advances are described by several examples for specific energy applications.

Introduction

Efficient production and consumption of energy has become a critical issue in the United States and around the world due to a number of factors, including increased demand due to rising population, depletion of fossil fuel sources, and detrimental impacts on the environment. Figure 1 shows the relative amounts of U.S. energy production and consumption by fuel source from 1949 to 2011 (Ref. 1), where it is apparent that fossil fuels and nuclear power have been the primary fuel sources. It has been estimated (Ref. 2) that world energy consumption will increase by 56% between 2010 and 2040. Although renewable energy and nuclear power are the world's fastest growing energy sources, fossil fuels will continue to supply almost 80% of world energy use through this time

period. As a result of this increase in energy consumption, carbon dioxide emissions from energy production are expected to increase significantly by approximately 46%, from 31 billion metric tons in 2010 to 45 billion metric tons in 2040.

These factors point to the need to produce and consume fossil and nuclear fuels with increased efficiency. Materials play an important role in these applications. For example, the efficiency of coal-fired power plants is most effectively improved with increases in the operating temperatures and pressures within the plant. New so-called "ultra super critical" power plants are currently being designed to operate at significantly higher pressures and

temperatures in order to realize these gains in efficiency. When plant efficiency is increased, more power can be generated with less consumption of coal and reduced carbon dioxide emissions. Successful implementation of these new plant designs hinges on the ability to develop materials with improved creep strength and corrosion resistance in order to provide adequate design lives out to about 30 years. Nickel-based alloys fill an important need in these new plants. In fact, in some cases Ni alloys provide the only suitable candidate material that can provide the required level of high-temperature strength and corrosion resistance.

There is a very wide range of Ni-based alloys that have been developed for an equally impressive range of applications. The extensive development and use of Ni-based alloys can, at least in part, be attributed to two unique characteristics. First, Ni is capable of dissolving high concentrations of alloying elements compared to other metals. The explanation for this dates back to some of the early work on the electron configuration of metals conducted by Pauling and has been attributed to the relatively full shell of d-band electrons in the Ni atom (Ref. 3). Second, the addition of Cr (and/or Al) to Ni provides excellent corrosion resistance resulting from the formation of a protective Cr_2O_3 (or Al_2O_3) surface oxide layer. This permits use of Ni-based alloys in a wide variety of applications that require protection due to various forms of degradation, such as aqueous corrosion, oxidation, and sulfidation. The subsequent discovery of improvements in creep strength provided by the addition of Ti and Al to promote precipitation of the ordered γ'-Ni_3(Ti, Al) phase extended the use of these alloys to applications requiring a combination of high-temperature strength and corrosion resistance.

While these attributes are certainly beneficial, the wide range and high concentration of alloying elements used in Ni-based alloys can present a challenge for

JOHN N. DuPONT is R. D. Stout Distinguished Professor, Department of Materials Science and Engineering, Lehigh University, Bethlehem, Pa.

KEYWORDS

Corrosion Resistance
Energy Production
Fossil Fuels
High Temperature
Nickel Alloys
Nuclear Energy

WELDING RESEARCH
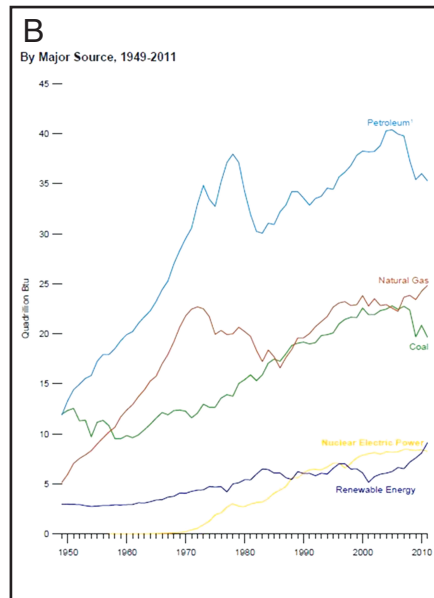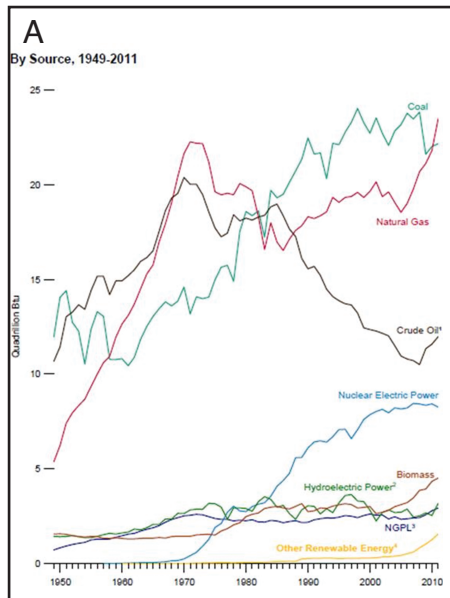
Fig. 1 — Relative amounts of U.S. energy production (A) and consumption (B) by fuel source from 1949 to 2011.
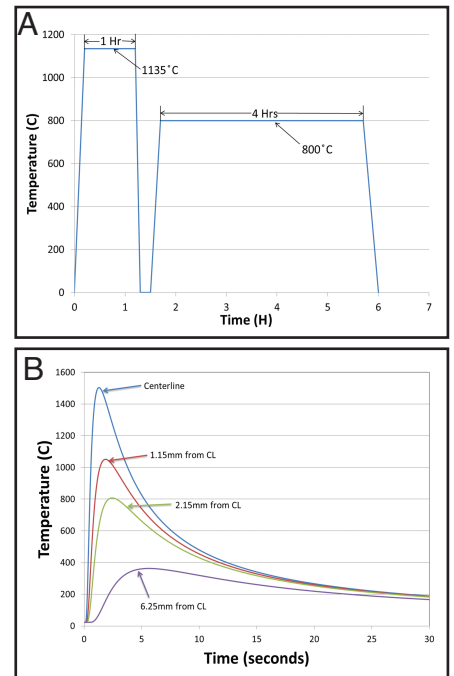

Fig. 2 — A — Typical heat treatment of the base metal for newly developed IN740 nickel-based superalloy; B — typical thermal cycle at various locations throughout a weld that are associated with fusion welding.

microstructure control during welding. The primary reason for this can be understood by comparing typical thermal cycles used for heat treatment during alloy production to those associated with welding. An example of this for the newly developed Ni-based superalloy IN740H is shown in Fig. 2. During alloy production, a heat treatment (Fig. 2A) is applied that consists of an initial hold at 1135°C for one h, followed by a water quench and re-heat at 800°C for four h. The initial high-temperature treatment is needed to homogenize microsegregation and dissolve secondary phases in the ingot. The quench is required to produce a single-phase austenite matrix that is supersaturated with respect to γ'-forming elements (Nb, Ti, Al). The final aging treatment at 800°C is used to produce a fine distribution of γ' precipitates that provide the best distribution and morphology for high-temperature strength. Figure 2B shows a typical thermal cycle for various locations throughout a fusion weld. Comparison of the weld thermal cycles to the original heat treatment thermal cycle reveals significant differences. The weld is exposed to a much wider range of temperatures (from above melting to ambient temperature) and time frames that are on the order of seconds (compared to hours for the original heat treatment).

The rapid weld thermal cycles associated with fusion welding cause significant alteration to the microstructure of fusion welds in Ni-based alloys, usually in a manner that has a negative effect on mechanical and corrosion properties. While progress is being made to develop new Ni-based alloys to meet future energy demands, the joining technology has not kept pace with the alloy development efforts. In most cases, the severe microstructural gradients in welds of Ni alloys lead to inferior properties that severely limit the overall performance of the component. Thus, it is critical that the joining technology progress in parallel with alloy development efforts so that these materials can be used in applications that require welding. This study describes several important applications of fusion welds in Ni-based alloys that are critical aspects to successful operation of various power plants. Examples include use of Ni-based weld cladding in conventional fossil-fired plants operating with low NOx burners, welding of new Ni-based superalloys for advanced coal-fired power plants, and welding of Gd-enriched nickel alloys for spent nuclear fuel applications.

Weld Cladding for Corrosion Control in Low-NOx Burners

In an effort to reduce boiler emissions, many coal-fired power plant operators have moved toward a staged combustion process. By delaying the mixing of fuel and oxygen, the amount of nitrous oxides (NOx) that are released as a by-product of combustion is reduced (Refs. 4, 5). Prior to this, most boiler atmospheres were oxidizing, allowing for formation of protective metal oxides on waterwall tubes made out of carbon- or low-alloy steels (Refs. 4, 6). Under those conditions, failure due to accelerated waterwall wastage was generally not a major problem. Staged combustion boilers, on the other hand, create a reducing atmosphere in the boiler due to the lack of oxygen. Sulfur compounds from the coal are transformed into highly corrosive gaseous H_2S (Ref. 7). In ad-

dition, corrosive deposits may form on the waterwall tubes due to the accumulation of solid particles in the combustion environment, such as ash and unburnt coal. As a result, low-alloy steels are often susceptible to excessive wastage rates and unsatisfactory service lifetimes (Refs. 4, 7). Thermal spray and chromium diffusion coatings were initially evaluated for protection in these environments, but generally do not provide adequate corrosion resistance. Commercially available nickel-based weld cladding is currently the industry standard for corrosion protection of waterwalls in boilers operating with low-NOx burners (Ref. 8). These alloys provide excellent resistance to general corrosion and can extend the service life of waterwalls relative to bare tubes. However, recent experience has shown that these coatings are susceptible to premature failure due to corrosion-fatigue cracking (Ref. 9). In fact, waterwall failures are the leading cause of forced outages of coal-fired power plants and can cost a utility company from $250,000 to $850,000 a day in downtime and lost revenue (Ref. 10).

Figure 3A is a photograph of an IN625 cladding that was applied with the gas metal arc welding (GMAW) process and removed from service due to the presence of extensive corrosion-fatigue cracking (Ref. 9). Figure 3B shows a cross-sectional photomicrograph of several small cracks that were examined early in the cracking stage, and Fig. 3C shows the distribution of alloying elements across the dendritic

substructure of the cladding. Figure 3D provides a lower magnification view that demonstrates the cracks initiate at the valleys of the weld ripples. The dendrite cores in the cladding exhibit a minimum in alloy concentration due to the relatively rapid solidification conditions associated with welding. As a result, the corrosion rate is accelerated in these regions and localized attack occurs at the dendrite cores. These localized penetrations form stress concentrations, which eventually grow into full-size fatigue cracks under the influence of residual and service-applied stresses, where the service-applied stresses arise primarily through thermal cycling. As shown in Fig. 3D, most cracks initiate at a region in the valley of surface weld ripple where an additional stress concentration exists. The high residual stress that results from welding also probably contributes to the cracking problem. In addition, dilution from the underlying steel tube substrate, which results in reduced alloy content of the cladding, compromises the corrosion resistance of the cladding.

The primary metallurgical factors that contribute to corrosion-fatigue cracking (weld ripples, microsegregation, high residual welding stresses, dilution) are all associated with the localized heating, melting, and solidification of the welding process. Thus, use of a coating that can be applied with more uniform heating in the solid state should help mitigate these problems and improve the cracking resistance. Work is in progress (Ref. 11) to evaluate coatings made by the coextrusion process in order to eliminate or reduce the inherent problems of weld cladding. With this process, a cylindrical shell of a corrosion-resistant alloy is first joined by explosive welding to a steel substrate, and the bimetallic billet is then coextruded at an elevated temperature to produce a tube with an outer coating. Since there is no melting/solidification involved, the coating microstructure consists of equiaxed grains with no microsegregation, similar to that expected for a wrought alloy.

The corrosion resistance of Alloys 600 (Ni-16Cr-8Fe) and 622 (Ni-22Cr-13Mo-2Fe) weld cladding and coextruded coatings have recently been compared using thermogravimetric testing in a simulated combustion gas ($10\%CO$-$5\%CO_2$-$2\%H_2O$-$0.12\%H_2S$-N_2, in vol-% at 600°C, and the results are shown in Fig. 4 (Ref. 11). A sample of wrought Alloy 600 was also tested. The coextruded coatings exhibit significantly better corrosion resistance compared to the weld cladding of the matching alloy. Figure 5 shows a weld cladding sample that was corrosion tested under solid-state conditions and then etched to reveal the dendritic substructure. Note that preferential corrosion has occurred at the dendrite cores (arrows).
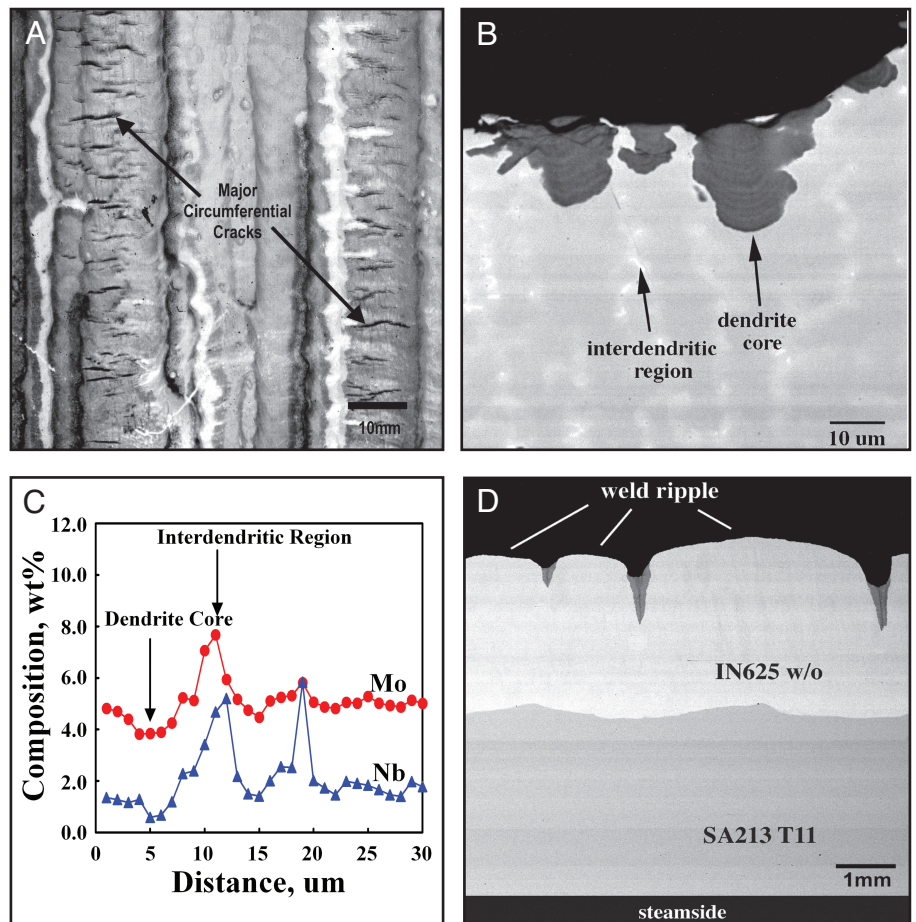
Fig. 3 — A — Photograph of a weld cladding with extensive circumferential cracks; B — cross-sectional scanning electron photomicrograph of several small cracks early in the cracking stage; C — distribution of alloying elements across the dendritic substructure of the cladding; D — photograph showing crack initiation at the valley of the weld ripple.

Figure 6 provides an EDS line scan that was acquired across the dendritic substructure of the weld cladding. As expected (Ref. 12), the dendrite cores are depleted in Mo, with Mo concentration levels down to ~ 11 wt-% (the nominal Mo concentration of the filler metal is ~ 13 wt-%). Figure 7 shows the microstructure of the coextruded coating, and an EDS line scan acquired across several grains of the coating is shown in Fig. 8. The coextruded coating exhibits a uniform, equiaxed grain structure and a uniform distribution of alloying elements.

For Alloy 600, the corrosion resistance of the wrought alloy and coextruded coating are comparable. This indicates that the coextrusion coating process has no adverse effect on the inherent corrosion resistance of the alloy. The improved corrosion resistance of Alloy 622 relative to 600 is attributed to the higher Cr and Mo content of Alloy 622. The difference in corrosion performance between the coating types can be attributed to two factors. First, the weld claddings evaluated in this work contain an additional 10 wt-% Fe from dilution with the steel substrate. This additional Fe stems from dilution with the underlying steel substrate and is always present in any weld cladding. The addition of Fe results in a corresponding decrease in the Cr and Mo content and often has a detrimental effect on corrosion resistance. The 10% dilution value used to prepare the sample for these tests represents a lower limit on the dilution level for commercially applied coatings. Such dilution effects do not occur with the coextruded coating. Second, the weld cladding exhibits microsegregation of alloying elements, resulting in preferential corrosion of the alloy-depleted dendrite core regions. The coextruded coatings also have a uniform coating thickness and smooth surface finish that should help reduce the localized stress concentrations that can aggravate the corrosion-fatigue problem. In addition, the heating and cooling cycles experienced during coextrusion are much less severe and more uniform compared to fusion welding, so the residual stresses should be significantly reduced.

While the mechanism of corrosion fatigue cracking is generally understood, there is a need to understand the corrosion fatigue behavior on a more fundamental basis in order to assess the relative
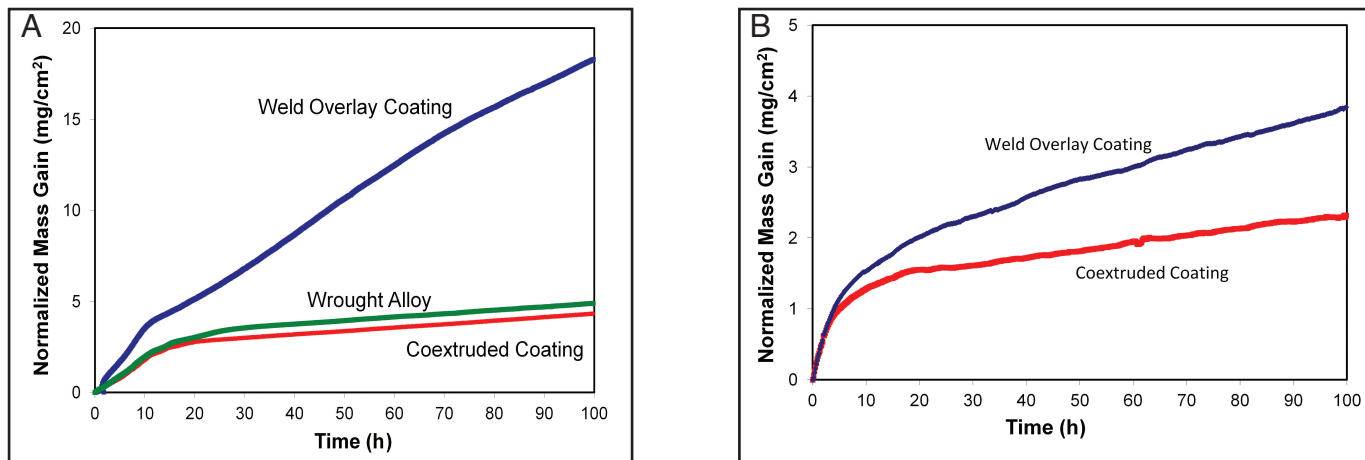
Fig. 4 — Thermogravimetric results from the gaseous corrosion testing for Alloy 600 (A) and Alloy 622 (B).
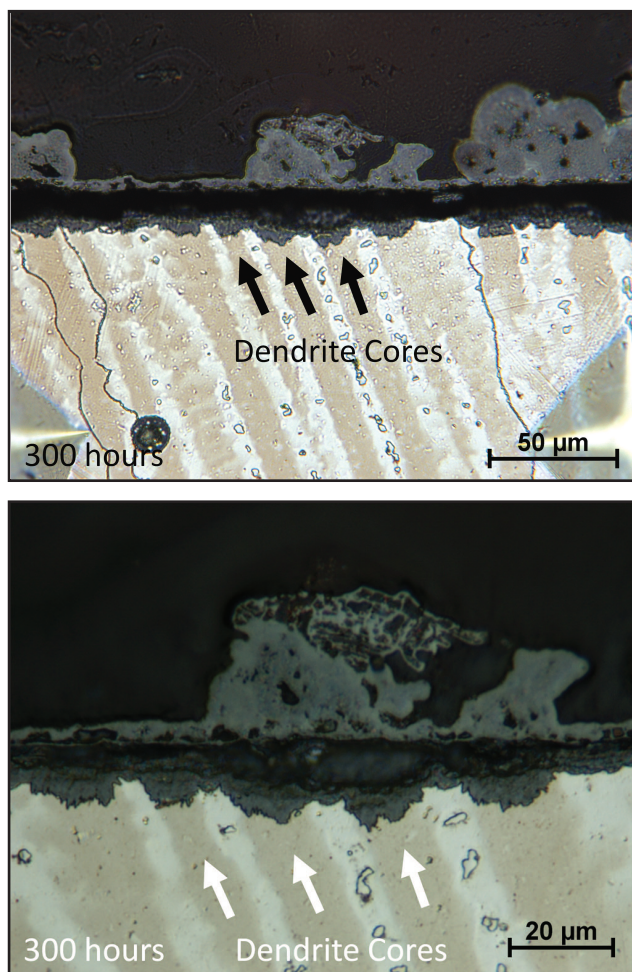
Fig. 5 — Light optical photomicrographs of the 300-h corrosion sample of the weld cladding after it was etched to reveal the dendritic substructure. Note that preferential corrosion has occurred at the dendrite cores (arrows).

cracking susceptibility of candidate alloys and coating processes. In order to accomplish this, an experimental technique needs to be developed that accurately simulates the corrosion fatigue mechanism of weld cladding in service. Typically, fatigue tests involve the use of standard specimen configurations such as compact tension (C(T)) or single edge-notched (SEN). These types of tests involve fatigue crack propagation using a single crack design. While this type of approach offers the ability to measure propagation rates of isolated cracks, it is not entirely adequate for studying the corrosion fatigue behavior of weld cladding in combustion conditions for several reasons. First, these approaches do not provide information on the corrosion fatigue crack initiation behavior of multiple cracks. Since crack initiation can comprise a large portion of the fatigue life, it is imperative that the crack initiation behavior be characterized. Additionally, single crack experiments do not take into account the effect of crack interactions on the crack propagation behavior. Numerous circumferential cracks form on the surface of Ni-based weld cladding during service (Refs. 9, 13). A series of cracks on the surface can alter the crack propagation behavior by reducing the stress intensity factors to a level well below that of a single isolated crack (Refs. 14, 15). Therefore, in order to understand the corrosion fatigue resistance, the effects of crack interactions need to be considered. This includes understanding the crack initiation behavior that affects the crack depths and distribution.

Figure 9 shows a recently developed corrosion fatigue cracking test apparatus involving a Gleeble thermomechanical simulator. With this test, a retort is positioned around the sample to allow the application of simulated combustion gases. The test sample is resistively heated to a constant temperature of 600°C, which is a typical surface temperature of Ni-based claddings in service. A representative (Refs. 16, 17) sulfidizing gas of N_2-10%CO-5%CO_2-0.12%H_2S circulated through the retort during the test. Corrosion fatigue tests to date have been conducted with an alternating stress profile involving a minimum tensile stress of 0 MPa and a maximum tensile stress of 300 MPa. The minimum and maximum stresses were alternated every five min (ten-min fatigue cycles). A maximum stress of 300 MPa was chosen because it is above the 200 MPa yield strength of Alloy 622 at 600°C. This was done to simulate the residual tensile stresses that develop in the waterwall tubes that cause significant yielding.

The validity of the experimental approach was first examined by comparing the laboratory-induced cracking mechanism to the established mechanism from field samples (Ref. 9). Figure 10A demonstrates the layered multiphasic scales that developed on the surface of the samples. An embryonic corrosion fatigue crack is shown, which formed within the multilayered corrosion scale. Figure 10B shows the initiation of a corrosion fatigue crack at a preferentially corroded dendrite core (the corrosion scale was removed by the etching process). These results are consistent with the corrosion fatigue mechanism observed on field samples. Figure 10C and D illustrates that the mature corrosion fatigue cracks propagated down the main axis of the dendrite cores and exhibit a secondary or "spinal" phase along the length
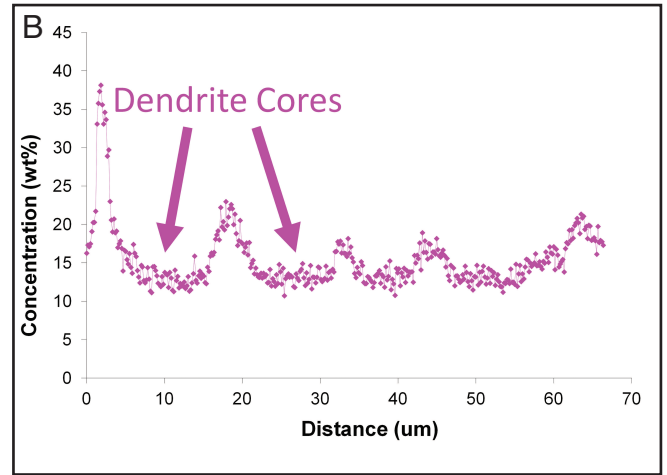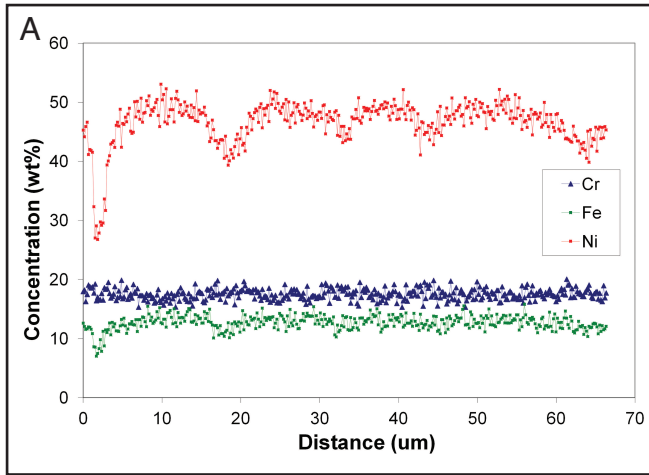
Fig. 6 — EDS line scan. A — Acquired across the dendritic substructure of the weld cladding showing the composition profiles for Fe, Ni, and Cr; B — acquired across the dendritic substructure of the weld cladding showing Mo depletion at dendrite cores.
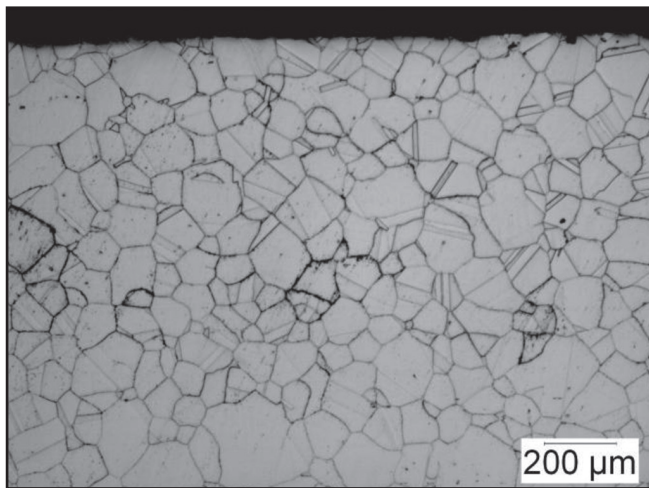

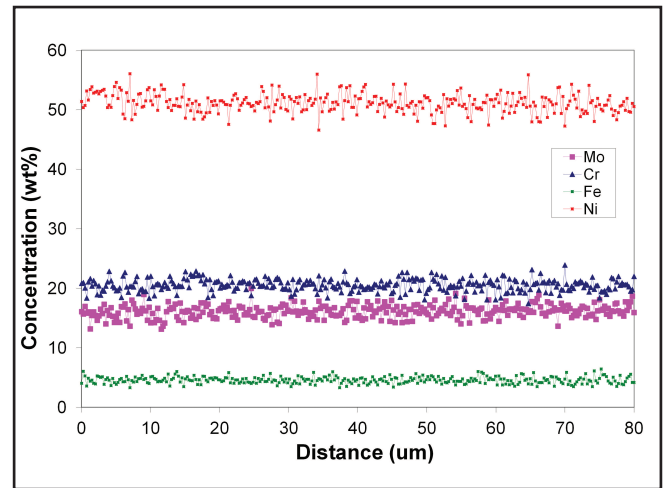*Fig. 7 — Light optical photomicrograph showing the microstructure of the coextruded coating.*

Fig. 8 — EDS line scan acquired across several grains of the coating.

of the crack. This is also consistent with the corrosion fatigue mechanism observed from examination of samples removed from the field. Figure 11 shows representative images of corrosion fatigue cracks in weld cladding samples tested out to 440 cycles. Figure 11A shows the presence of a small corrosion fatigue crack after 25 cycles. This observation indicates that corrosion fatigue cracks initiated relatively quickly as a result of the accelerated test conditions. Thus, the experimental approach was able to accurately reproduce the corrosion fatigue mechanism in a relatively short amount of time. Additionally, multiple corrosion fatigue cracks were apparent within each of the samples after 25 cycles, indicating that cracks continuously formed throughout the test. The variation in the corrosion fatigue crack depths with increasing number of corrosion fatigue cycles further supports this conclusion. Serial sectioning and quantitative image analysis techniques have recently been used to measure the frequency and depths

of corrosion fatigue cracks that develop during this test. As an example, Fig. 12 compares the maximum crack depths of a cladding applied with the GMAW process to that of a laser weld cladding. Note that the laser weld cladding exhibits better performance than the GMAW cladding in terms of both time to crack initiation and crack depth for a given number of cycles. Work is currently in progress to understand the microstructural differences that account for this improvement in corrosion-fatigue cracking resistance and to test other coating systems, such as the coextruded coating described above.

Welding of IN740H for Ultrasuper critical Power Plants

As described above, advanced ultra-supercritical (AUSC) power plants are currently being designed to operate at higher pressures and temperatures for increased efficiency. These more aggressive operating conditions place heavy demands

on tubing and piping components within the plants, particularly with regard to creep resistance. Figure 13 (Ref. 18) shows the maximum allowable stress as a function of temperature for a wide range of stainless steels and nickel alloys. The temperatures and pressures associated with AUSC conditions are expected to be ~ 1300° –1400°F (704° –760°C) and 4500 lb/in.[2] (31 MPa), respectively. Note that these operating conditions lie on the upper bound of allowable stresses and temperatures even for the commonly used solid solution strengthened Ni alloys. This situation represents a significant challenge to the successful implementation of these newer, more efficient plants. In response to this need, a new precipitation-strengthened nickel-based superalloy has recently been developed known as IN740H. This alloy has significant additions of Nb, Ti, and Al in order to form the γ' precipitate for high-temperature creep strength. Extensive fabrication by fusion welding will be required on this alloy during plant con-
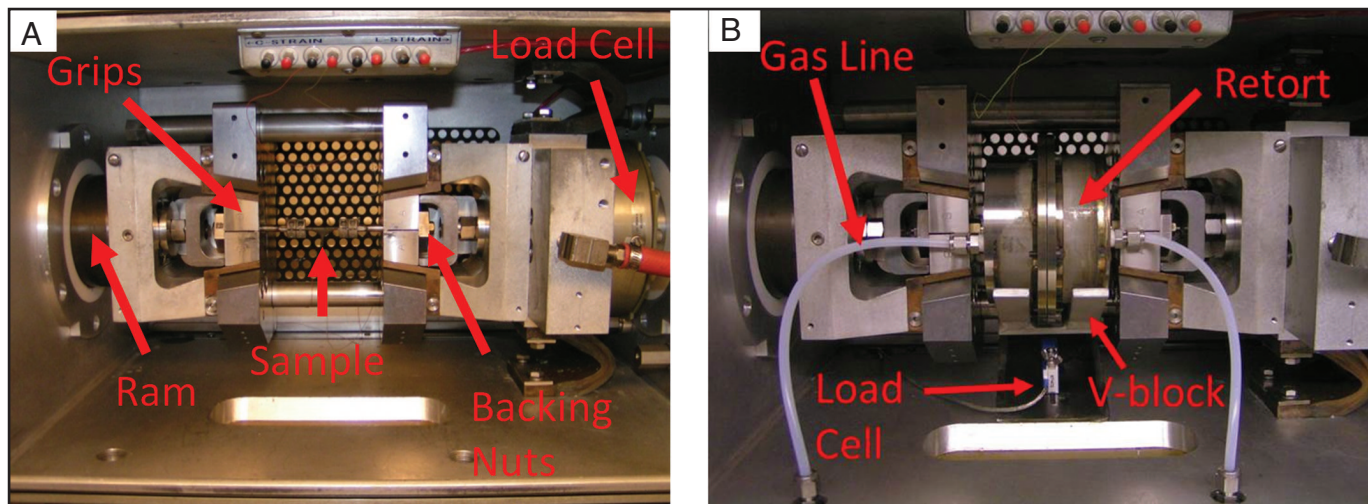
Fig. 9 — A — A corrosion fatigue sample that has been clamped into the grips of the Gleeble; B — the retort that has been designed to seal around a corrosion fatigue sample and allow for the application of corrosive gas.
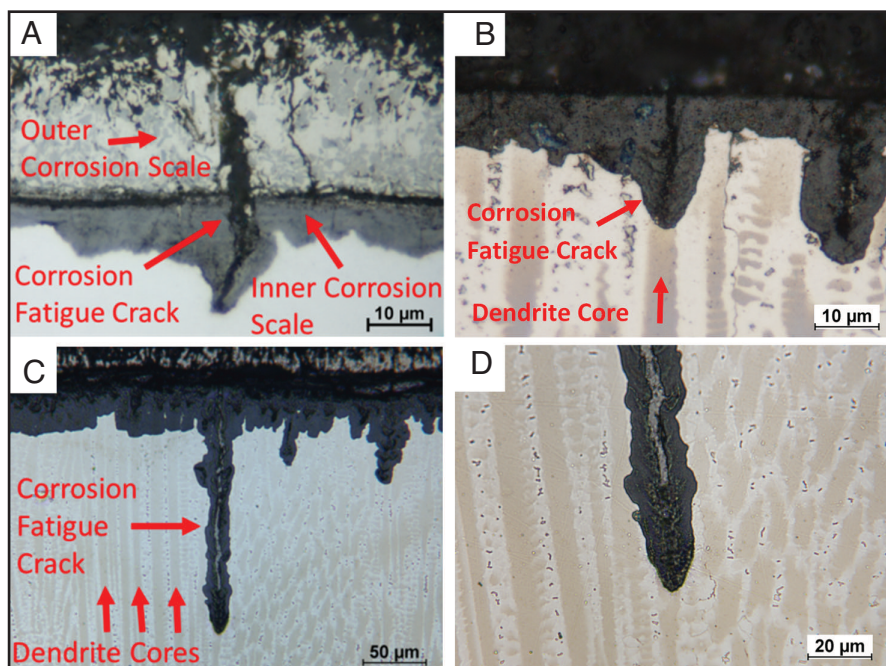
Fig. 10 — A — Multilayer corrosion scale that develops under the simulated combustion conditions; B — corrosion fatigue cracks initiating at the alloy-depleted dendrite cores. (The etching process removed the corrosion scale on the surface of the sample); C, D — a mature corrosion fatigue crack that propagated down a dendrite core. A secondary phase was observed along the length of crack.

struction and subsequent maintenance. Thus, retention of the creep properties of the welds is of primary importance.

Figure 14 shows recent results from Oak Ridge National Laboratory (Ref. 19) that compares the stress rupture properties of wrought IN740H tube material to that of cross-weld samples, where a significant reduction in the weld metal creep life is apparent. These results have required the use of a weld strength reduction factor for the welds of 0.70, which can place rather appreciable restrictions on the load-bearing capacity of welded components. Thus, it is important to understand the cause of this reduced creep strength so

that a viable solution can be developed.

Electron microscopy techniques have recently been used (Refs. 20, 21) to characterize both base metal and weld samples exposed to a wide range of creep test conditions in order to identify the cause for the reduced creep life in the welds. Figure 15 compares scanning electron microscopy (SEM) photomicrographs of base metal and weld samples after creep testing. The base metal sample exhibits a uniform distribution of γ' precipitates directly up to the grain boundary. In contrast, the weld metal has precipitate-free zones (PFZs) at the grain boundaries, and the creep voids that initiate premature failure in the weld

are commonly observed to initiate at the PFZs. The localized creep-failure along these PFZs is generally attributed to their lower strength due to the lack of a dense population of fine γ' precipitates. The presence of PFZs in creep-resistant alloys has been observed in many alloy systems and been attributed to a number of different formation mechanisms, including stress-assisted diffusion associated with Nabarro-Herring (NH) creep conditions, grain boundary carbide formation, and discontinuous precipitation/coarsening (DPC) (Refs. 22–34). Each mechanism is associated with a set of unique microstructural features that can be used to identify the responsible mechanism, which is critical for formulating a solution. While a complete review of these mechanisms is beyond the scope of this paper, several distinguishing characteristics are worthy of discussion.

Nabarro-Herring creep and grain boundary carbide formation will each produce PFZs that are symmetric about the grain boundary. In addition, the coarse secondary phases within the PFZs typically exhibit a globular morphology. Precipitate-free zones formed under NH creep conditions have the added feature of being dependent on the direction of applied stress, where the PFZs will form normal to the applied stress direction. In contrast, PFZs that form due to DPC exhibit a lamellar morphology and are asymmetric about the grain boundary (i.e., the PFZ will be confined to one grain). These features are the result of precipitation (or coarsening) in the presence of a moving boundary. Figure 16 shows the lamellar morphology that is commonly observed with the PFZs in welds of IN740H that have been creep tested. Transmission electron miscroscope techniques have been used to confirm that the coarse secondary
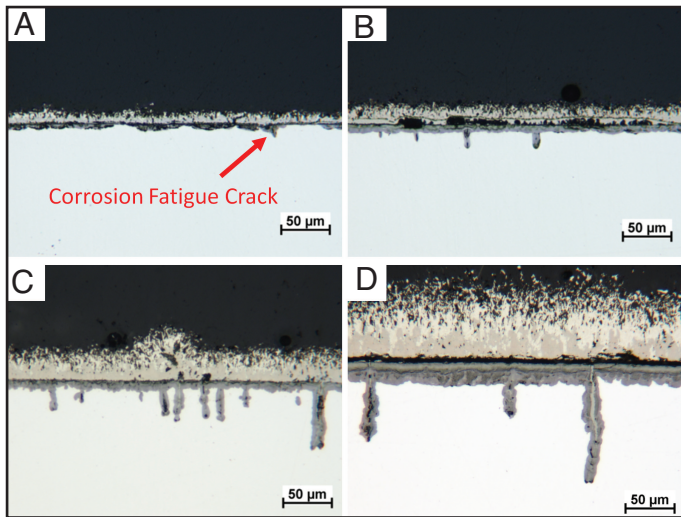
Fig. 11 — Corrosion fatigue cracks observed in the GMAW cladding. A— 25 cycles; B — 50 cycles; C — 100 cycles; D — 442 cycles.
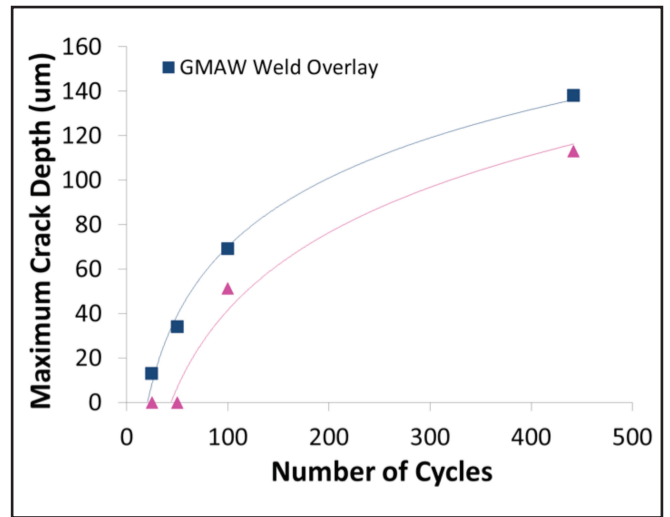

Fig. 12 — A — Average crack depths; B — maximum crack depths for the GMAW and laser weld cladding samples.
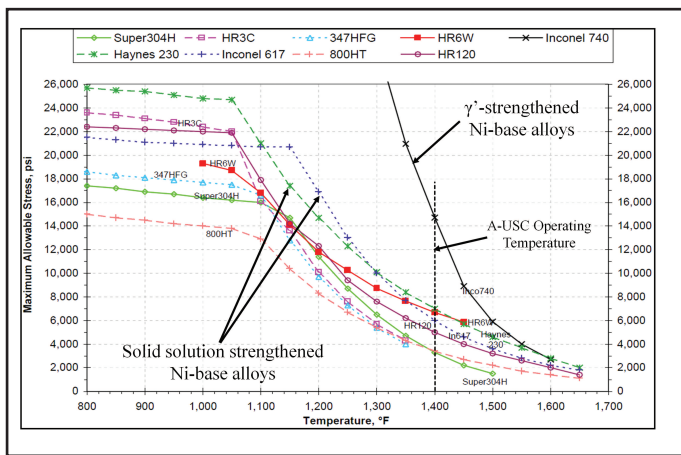

Fig. 13 — Maximum allowable stress as a function of temperature for a wide range of stainless steels and nickel alloys.
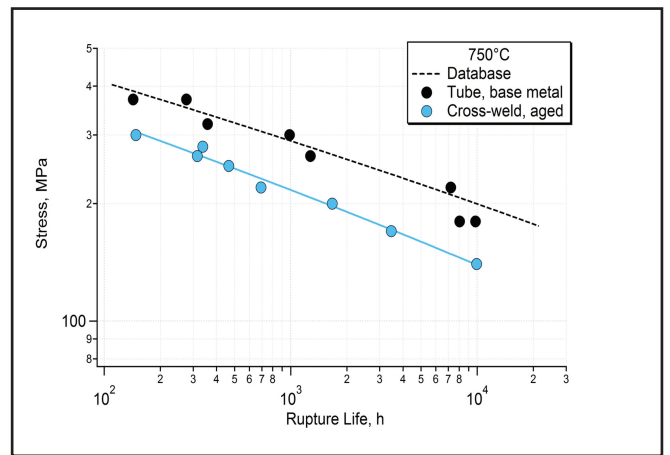

Fig. 14 — Recent results from Oak Ridge National Laboratory that compares the stress rupture properties of wrought IN740H tube material to that of cross-weld samples.

phase within the PFZ is γ'. Figure 17 shows electron backscattered diffraction (EBSD) patterns acquired across the boundary that contains a PFZ. The EBSD patterns demonstrate that the PFZ is located entirely in Grain 2. Detailed comparisons of creep samples from a wide range of test conditions also showed that there was no relation between the PFZ orientation to that of the applied stress. It is worth noting that similar PFZs are occasionally observed in the base metal of IN740H after creep. However, the base metal requires significantly longer times (or higher temperatures) for PFZ formation. Thus, the reduced creep strength in welds of IN740H can be attributed to enhanced susceptibility to PFZ formation associated with DPC.

The enhanced driving force for PFZs in the weld metal can be understood with reference to Figs. 18 and 19. Figure 18 shows results from EDS traces acquired

across the dendritic substructure of the weld. The data points reflect the average and standard deviation from multiple measurements, while the lines represent results from Scheil solidification simulations (Ref. 20). Note there is good agreement between the model and experimental results. In this case, the calculations are probably more reflective of the actual compositions within the very edge of the interdendritic regions due to the spatial resolution limitations of the electron beam (which is about 1 μm^3) and the large concentration gradient within the interdendritic region. The results also show that, due to microsegregation, the concentrations of Ti and Nb are higher at the grain boundary and interdendritic regions (the Al concentration is also slightly higher). The increased localized concentration of these γ' forming elements is important, since it causes an increased supersaturation beyond the solubility

limit, thus leading to the enhanced grain boundary precipitation shown in Fig. 19. Classical solutions to the diffusion equations associated with precipitation (Ref. 35) reveal that the growth rate of the precipitate/matrix interface is directly proportional to the degree of supersaturation in the matrix, ΔC_O. Here, ΔC_O can be viewed as the driving force for precipitation and is given by the difference between the actual matrix concentration and the solubility limit at a given temperature. Figure 20 shows the ΔC_O values (at 800°C, the typical operating temperature) associated with the γ' forming elements Nb, Ti, and Al that demonstrate the significantly enhanced driving force for precipitation associated with interdendritic microsegregation. Also note from Fig. 19 that there is significant grain boundary curvature. This could be associated with the original (nonequilibrium) grain boundary curvature typical in the as-solidified condition,
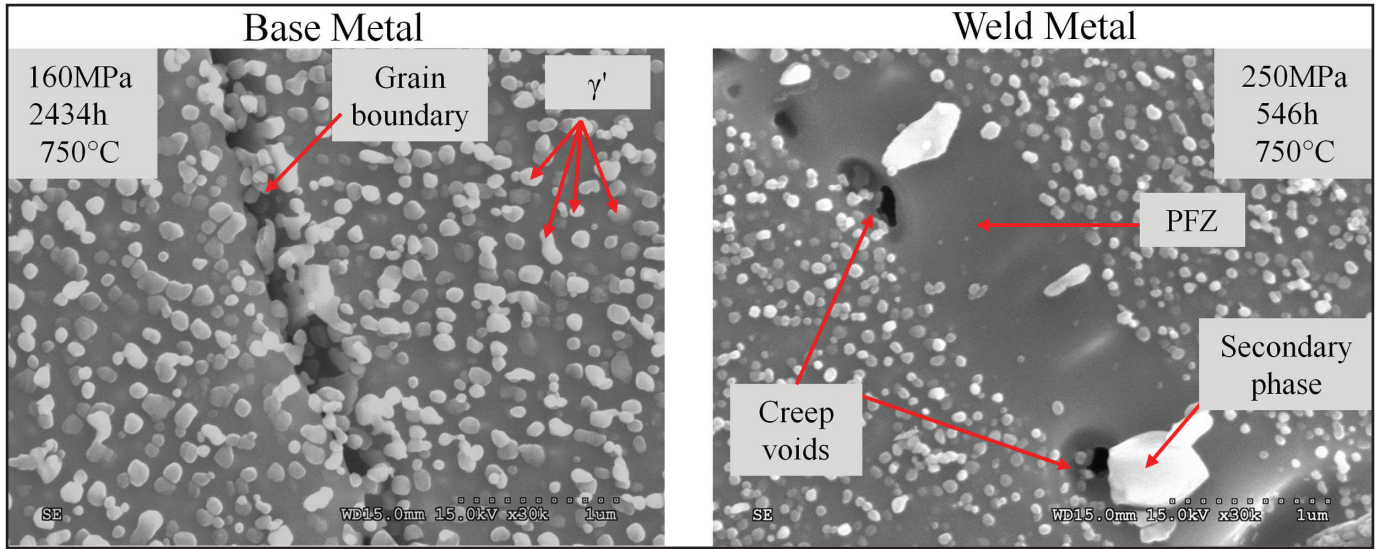
Fig. 15 — Scanning electron microscopy photomicrographs of base metal and weld samples of Alloy IN740H after creep testing.
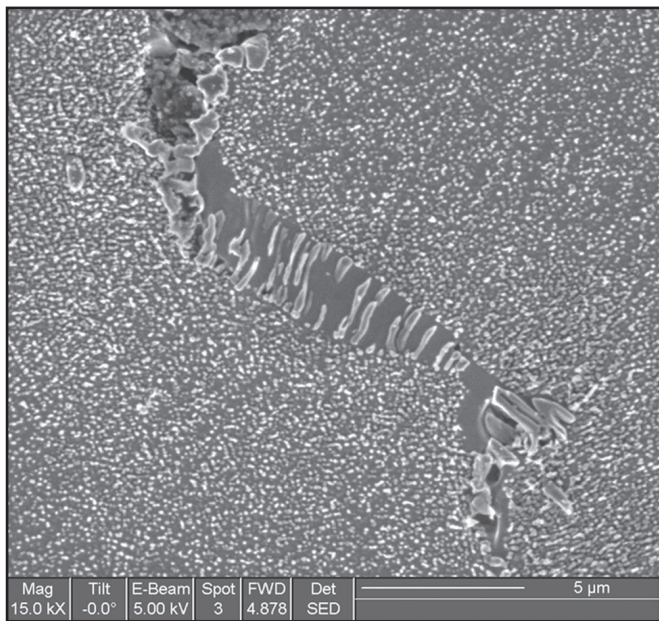

Fig. 16 — Scanning electron microscope photomicrograph showing the lamellar morphology that is commonly observed with the PFZs in welds of IN740H that have been creep tested.

which would then provide the driving force for boundary movement. The observed curvature could also possibly be the result of the DPC process itself. Work is in progress to more clearly understand the factors leading to boundary migration.

Work is also in progress to explore new filler metal compositions that should be more resistant to the formation of PFZs during creep. Meanwhile, the results presented above demonstrate that a postweld heat treatment (PWHT) that homogenizes microsegregation within the weld may help to minimize the problem of PFZ formation. Dissolution of secondary phases that form during solidification may also be helpful. In light of this, it is important to establish the influence of time and temperature on the homogenization kinetics of welds in IN740H. A study in this area has recently been completed and is summarized below (Ref. 20).

The most convenient PWHT would permit dissolution of secondary phases and homogenization in a single initial step, followed by a subsequent aging treatment. However, it must be recognized that the local increases in solute concentration within the interdendritic regions will cause a corresponding decrease in the local solidus temperature. This, in turn, could lead to localized melting within the solute-enriched interdendritic regions if the initial PWHT is too high. This is demonstrated in Fig. 21, which shows the stability of various
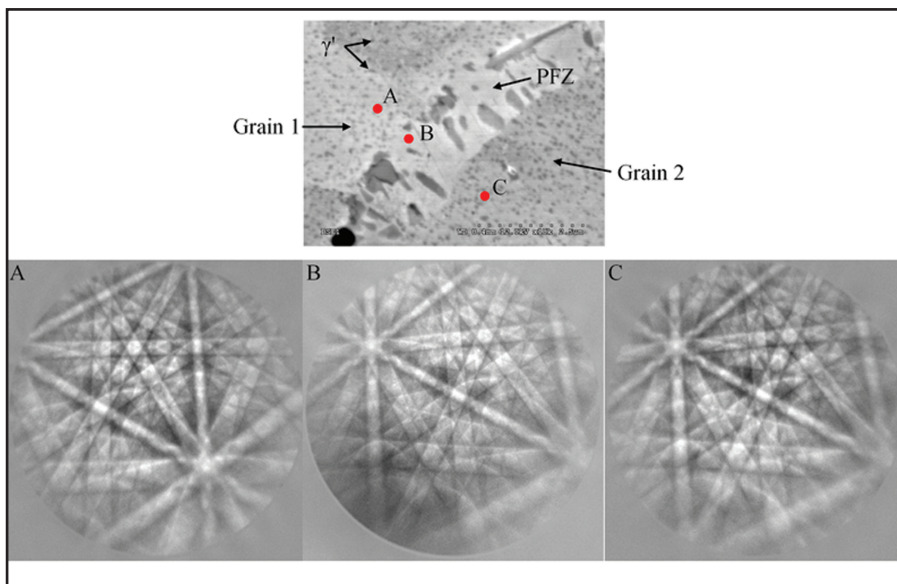

Fig. 17 — Electron backscattered diffraction (EBSD) patterns acquired across the boundary of a weld in IN740H that contains a PFZ. The EBSD patterns demonstrate that the PFZ is located entirely in Grain 2.
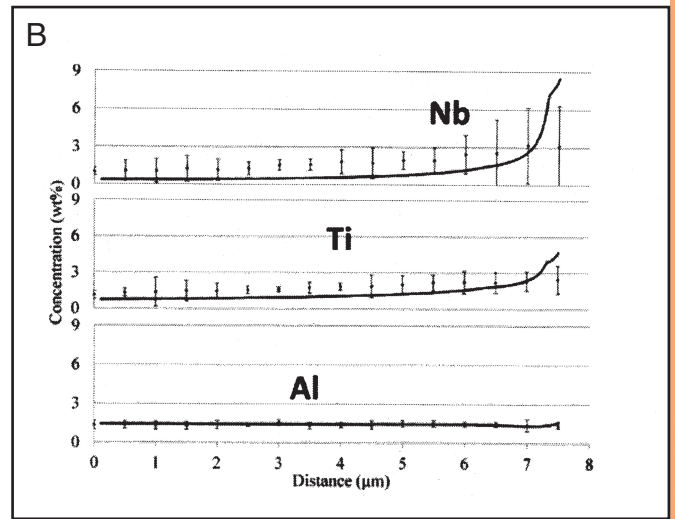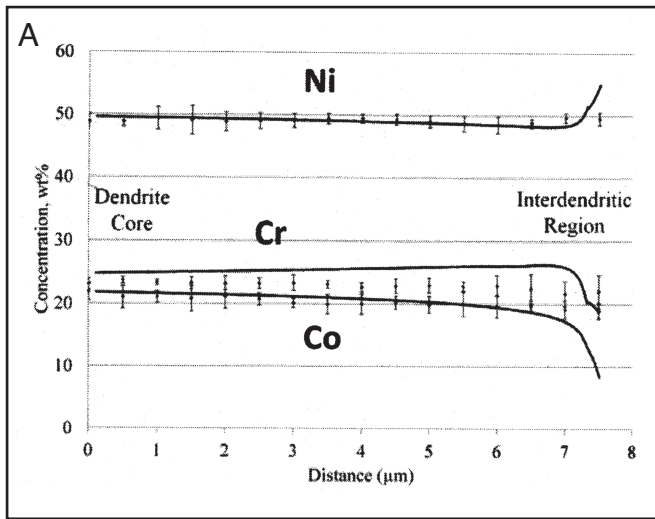
Fig. 18 — EDS traces acquired across the dendritic substructure of a weld in IN740H. The data points reflect the average and standard deviation from multiple measurements, while the lines represent results from Scheil solidification simulations.
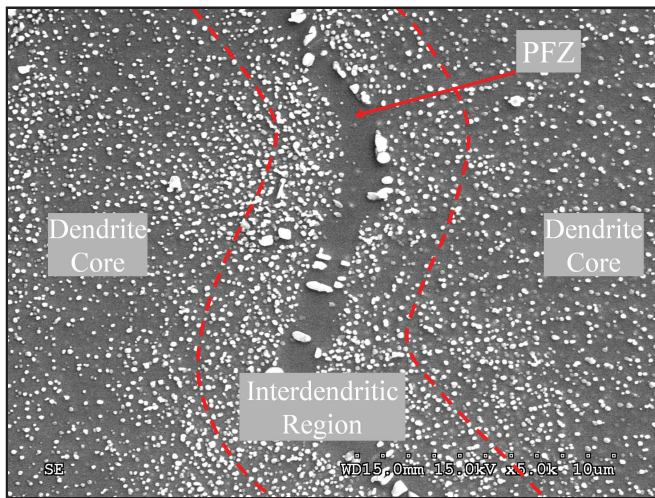

Fig. 19 — SEM photomicrograph showing how increased localized concentration of γ'-forming elements produces enhanced grain boundary precipitation in fusion welds on Alloy IN740H.
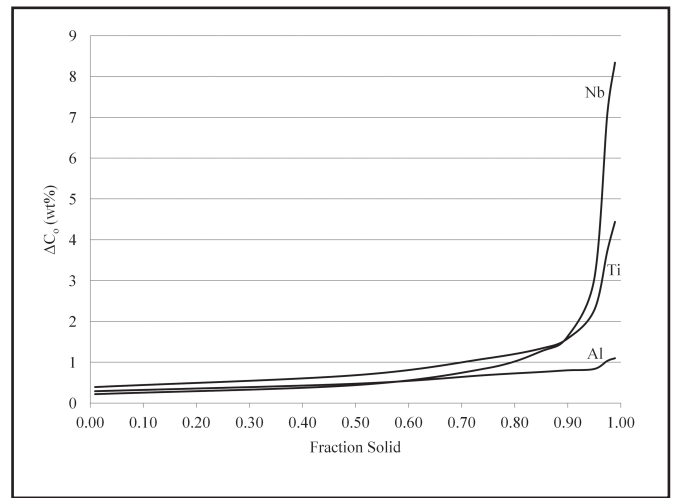

Fig. 20 — ΔC_O values at 800°C associated with the γ'-forming elements Nb, Ti, and Al that demonstrate the significantly enhanced driving force for precipitation in the interdendritic regions of welds in Alloy IN740H.

phases as a function of temperature in IN740H for the base metal nominal composition (Fig. 21A, B) and for a value of 0.99 fraction solid that is representative of the interdendritic composition — Fig. 21C, D. (Figure 21B, D shows the same results as Figs. 21A and 22C, but over a narrower temperature range for clarification.) Note that, if the heat treatment was based on the nominal composition of the base metal, the results suggest that the initial PWHT step could be conducted slightly beyond 1300°C before any problems from localized melting (also note that the MC carbide will still be stable at these high temperatures). However, when dendritic segregation is properly considered (Fig. 21C, D), the results demonstrate that the initial PWHT temperature should not exceed about 1150°C to avoid localized melting in the interdendritic regions. These

results emphasize the importance of designing PWHT schedules based on the actual phase stability in the fusion zone as affected by compositional gradients.

Figure 22 shows the results of DIC-TRA calculations for IN740H that demonstrate the homogenization kinetics. Results are shown for the concentration gradient of Nb, since this is the slowest diffusing element in the system and therefore the rate-limiting step. The calculations show that a PWHT at 1100°C for four h should eliminate the microsegregation, and this has been confirmed by experimental measurements (Fig. 23). Once the homogenization is complete, a higher temperature solution temperature can be utilized if needed for more complete dissolution of secondary phases. Although it is recognized that the 1100°C/4-h treatment is not practical for a PWHT con-

ducted in the field, the results can be applied to shop fabrication conditions. As mentioned previously, the potential for a more practical solution through design of tailored filler metals is needed and is currently being pursued.

Fusion Welding of Gd-Enriched Ni Alloys for Spent Nuclear Fuel Applications

Nuclear fuel plays an important role in energy production in the United States and throughout the world, and the use of nuclear power is expected to rise over the coming years. One of the major challenges associated with nuclear fuel is the handling of spent nuclear fuel (e.g., nuclear waste). Safe disposition of spent nuclear fuel requires the development of thermal neutron-absorbing structural materials for
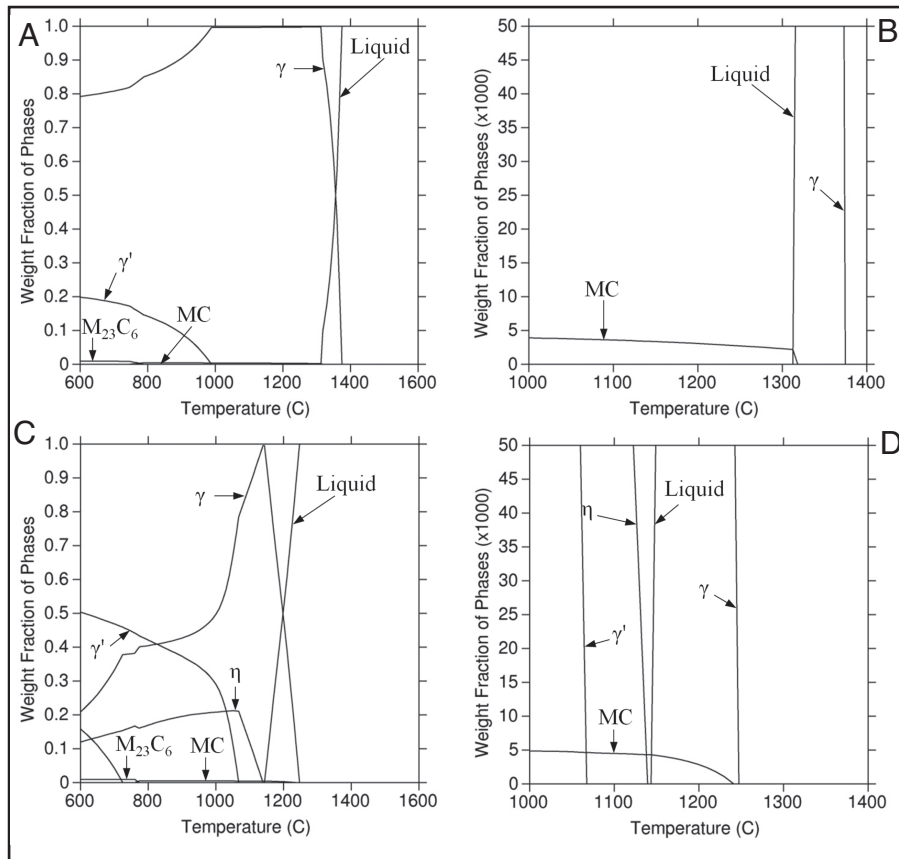
Fig. 21 — *Stability of various phases as a function of temperature in IN740H for the base metal nominal composition (Fig. 21A, B) and for a value of 0.99 fraction solid that is representative of the interdendritic composition (Fig. 21C, D) in fusion welds.*

Fig. 22 — *DICTRA calculations for IN740H that demonstrate the homogenization kinetics. Results are shown for the concentration gradient of Nb, since this is the slowest diffusing element in the system and therefore the rate-limiting step.*

nuclear criticality control. These materials will be used for the internal baskets that separate spent fuel assemblies and are required for structural support, spent nuclear fuel geometry control, and nuclear criticality safety. Given the large quantity of material required for this application, the material should be producible with conventional fabrication methods such as ingot casting and hot working. Ultimately, the material will be formed and welded into an internal structure that will cradle the fuel and maintain a specified geometry, so the material must also exhibit good weldability.

Recent research (Refs. 36–38) has focused on development of gadolinium-(Gd) enriched Ni-based alloys for this application. Gd serves as an effective alloy addition for this application because it has a very high neutron absorption cross section (Refs. 23, 39). The results of recent research has also shown that Gd additions at the nominal 2 wt-% level can successfully be added to the commercial Ni-based C-4 alloy while maintaining adequate hot workability, weldability, and mechanical properties.

The current plan for fusion welding of this alloy involves the use of a Gd-free commercial filler metal such as Alloy C-4 or 59. With this approach, the Gd content

in the fusion zone will vary with weld metal dilution, and the dilution level is strongly affected by the welding parameters (Refs. 40, 41). Considering the case in which a base metal containing 2 wt-% Gd is welded with a Gd-free filler metal, the concentration of Gd in the fusion zone will vary linearly with dilution and can be close to 0 wt-% Gd (at low dilution values) to 2 wt-% Gd (for an autogenous weld in which the dilution is 100%). The welding parameters are typically selected based on the required weld size and joint design requirements, and a wide range of welding parameters can be expected in practice. This, in turn, can produce a wide range of fusion zone Gd concentration values. The Gd concentration can also vary throughout the fusion zone of a given weld in multiplepass welding applications. Recent research has shown that Gd controls the solidification behavior of this alloy. In particular, the solidification temperature range and amount of terminal eutectic-type constituents that form at the end of solidification are essentially dominated by the Gd concentration (Ref. 38). In addition, it has also been well established that the solidification cracking susceptibility is also strongly affected by the solidification temperature range and amount of terminal eutectic-type constituents that form
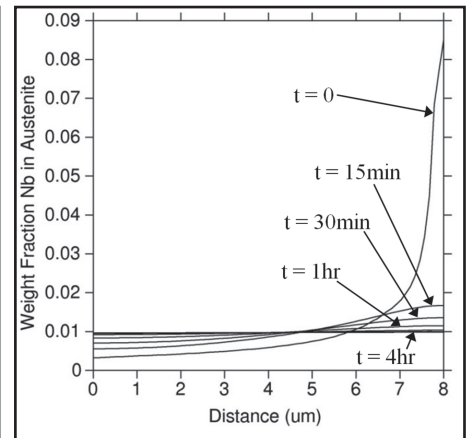
during solidification of the fusion zone (Refs. 42, 43). Thus, it is important to determine the influence of Gd concentration on the solidification cracking susceptibility of Alloy C-4 so that these structural materials can be welded while maintaining their structural integrity.

Figure 24 shows the influence of Gd on the solidification cracking susceptibility of Alloy C-4. The cracking susceptibility is low for the Gd-free base alloy. The cracking susceptibility then increases with increasing Gd concentration up to ~1 wt-% Gd and then decreases to a level that is similar to the base alloy at Gd concentrations of 1.5 to 2.5 wt-%. Typical microstructures of the Varestraint samples are shown in Fig. 25. No significant crack healing due to backfilling of solute-rich liquid occurred in the alloy with 1.01 wt-% Gd. Similar results were obtained with the alloy that had 0 and 0.46 wt-% Gd. However, a significant amount of crack healing was observed in the alloys that had additions of Gd at the 1.49 wt-% level and above.

The Varestraint weldability results show that the cracking susceptibility reaches a maximum at ~ 1 wt-% Gd, and decreases with both higher and lower Gd additions. Previous research (Refs. 42, 43) has shown that the solidification cracking susceptibility of engineering alloys is strongly affected by the solidification temperature range and amount of terminal eutectic-type constituent that forms at the end of solidification. Solidification of these alloys initiates at the liquidus temperature by the formation of primary γ–austenite. Essentially, no Gd is dissolved in the austenite matrix. Thus, as solidification proceeds, the liquid becomes increasingly enriched in Gd until the Liquid → γ + Ni₅Gd eutectic-type reaction is reached, at which point solidification is terminated.
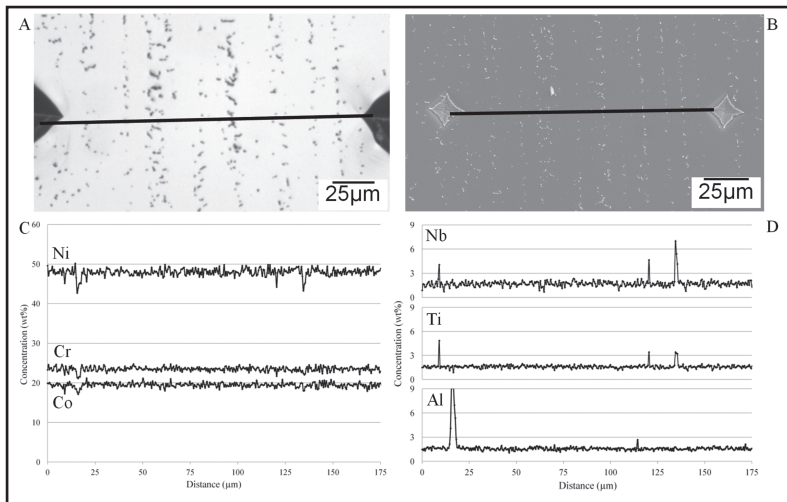
Fig. 23 — Semiquantitative (standardless) XEDS line scan across dendrites in a single-pass GTA weld of Alloy 740H after homogenization at 1100°C for 4 h. A — Light optical micrograph of region of interest; B — SEM micrograph of region of interest; C — concentration profile for major alloying elements; D — concentration profile for γ′-forming elements.
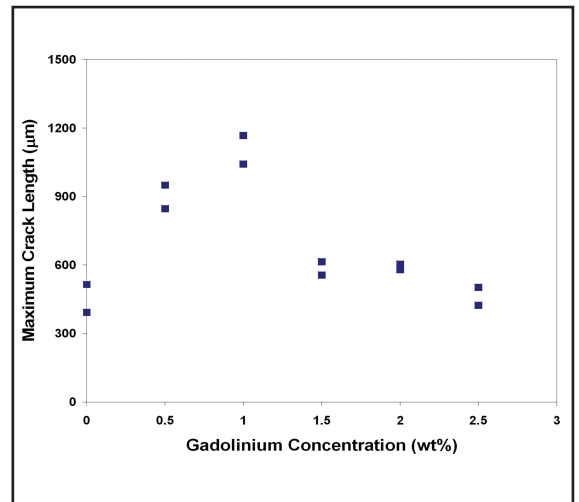
Fig. 24 — Varestraint results showing maximum crack length as a function of Gd concentration in Alloy C-4.

This reaction sequence and temperature range is generally similar to that expected in the binary Ni-Gd system. Simple binary Ni-Gd alloys with less than about 13 wt-% Gd exhibit a similar two-step solidification sequence consisting of primary austenite formation followed by a terminal eutectic reaction involving the $Ni_{17}Gd_2$ intermetallic at 1275°C (Ref. 44). By comparison, the multicomponent Ni-Cr-Mo-Gd alloys examined here complete solidification at ~ 1258°C by a terminal eutectic-type reaction involving the Ni_5Gd intermetallic. Thus, although the secondary phase within the terminal eutectic constituent is different in each case, the terminal reaction temperatures are very similar. In fact, as shown in Fig. 26, a pseudo binary solidification diagram has recently been developed (Ref. 38) for this alloy that is similar to the phase diagram of a binary eutectic alloy. In this case, the "solvent" is represented by the Ni-Cr-Mo solid solution γ-austenite phase and Gd is treated as the solute element. Although the diagram does not account for the minor variation in matrix Mo concentration that occurs due to microsegregation, the similarity of this γ-Gd binary system to a binary eutectic system is readily evident in several ways, including the as-solidified microstructure consists of primary γ dendrites surrounded by an interdendritic eutectic-type constituent in which the secondary phase in the eutectic is solute rich; the amount of eutectic-type constituent increases with increasing solute content; and the proportional amount of each phase within the eutectic constituent is relatively insensitive to nominal solute content (Ref. 38). Also note that the eutectic temperature is not strongly dependent on the nominal Gd-concentration.

The pseudo binary diagram developed for these alloys is useful for interpreting the weldability results because it permits direct determination of the solidification temperature range and amount of terminal γ/Ni_5Gd eutectic constituent as a function of Gd concentration. The fraction of terminal γ/Ni_5Gd eutectic constituent (f_e) that forms during solidification can be calculated with the Scheil equation (Ref. 45) via

$$f_e = \left[\frac{C_e^{Gd}}{C_o^{Gd}}\right]^{\frac{1}{k-1}}$$

(1)

where C_e^{Gd} is the concentration of Gd in the liquid at the eutectic reaction (14.7 wt-% Gd, Fig. 26), C_o^{Gd} is the nominal Gd concentration, and k is the distribution coefficient for Gd. Equation 1 is valid for conditions in which the diffusivity of solute (Gd) in the solvent (γ) is insignificant. Previous work (Ref. 37) has shown that essentially no Gd is dissolved in the γ matrix, which results in the equivalent condition of negligible solute diffusivity in the solvent. The lack of Gd solubility in austenite also indicates that k for Gd is 0, and Equation 3 reduces simply to

$$f_e = \frac{C_o^{Gd}}{C_e^{Gd}}$$

(2)

The solidification temperature range of fusion welds is best represented by the separation between the on-heating liquidus temperature (T_L) and on-cooling eutectic temperature (T_e) because solidification initiates epitaxially at the weld interface without the need for undercooling (Refs. 46, 47). As mentioned previously

and discussed in more detail elsewhere (Ref. 38), the eutectic temperature (T_e) does not vary significantly with Gd concentration and can be represented by an average value of T_e = 1258°C. The liquidus line in Fig. 26 can be expressed by a simple linear equation of the form

$$T_L = T_o + m_L C_o^{Gd}$$

(3)

where T_o is the melting point of the Ni-Cr-Mo "solvent" and m_L is the liquidus slope. Linear regression analysis of the phase diagram leads to values of T_o = 1422°C and m_L = –11.2°C/wt-% Gd. Thus, the solidification temperature range (ΔT) can be directly determined as a function of Gd concentration via

$$\Delta T = T_o + m_l C_o^{Gd} - T_e$$

(4)

The solidification temperature range is important from a weldability perspective because it controls the size of the solid + liquid "mushy" zone that trails the fully molten weld pool. Assuming a constant temperature gradient in the solid + liquid region (i.e., fixed welding parameters and sample size/geometry), the size of the mushy region is given simply by the ratio of the solidification temperature range to temperature gradient. Thus, alloys with narrow solidification temperature ranges are generally crack resistant because the mushy zone is relatively small. The influence of the amount of terminal eutectic liquid is a bit more complicated. At very low amounts of terminal liquid, the cracking resistance is generally not adversely affected because there is not enough liquid to cover the solidification grain boundaries and interdendritic regions. Thus, solid-solid boundaries can be easily
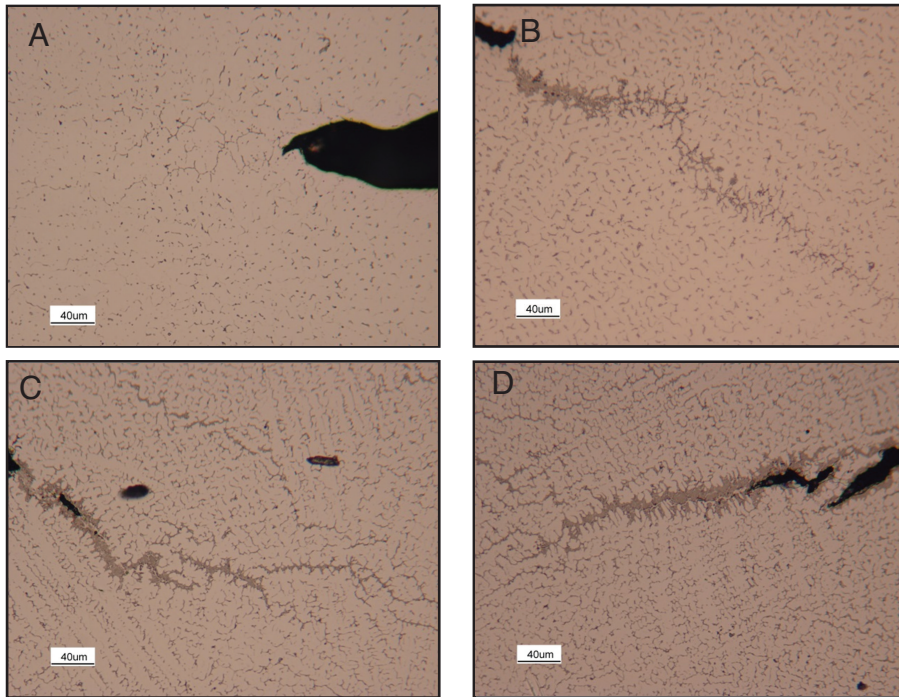
Fig. 25 — Microstructures of the Varestraint samples from Alloy C-4 alloyed with various concentrations of Gd. A — 1.01 wt-% Gd; B — 1.49 wt-% Gd; C — 1.90 wt-% Gd; D — 2.45 wt-% Gd.

Fig. 26 — Pseudo-binary solidification diagram developed for Gd-enriched Alloy C-4.

established without interference from the liquid, and the cracking resistance is generally good. (The presence of surface-active elements that modify the solid/liquid surface energy and promote extensive wetting of the boundaries by the liquid at even small liquid fractions can alter this general trend.) As the fraction of terminal eutectic liquid increases, the liquid more extensively wets the boundaries, thus interfering with the formation of solid-solid boundaries and causing an increase in the cracking susceptibility. At considerably higher fractions of liquid, backfilling of cracks can occur by the liquid and heal the cracks as they form. This phenomenon is similar to liquid feeding by risers used to control solidification shrinkage defects in castings.

With this background in mind, the influence of Gd concentration on the cracking susceptibility, amount of terminal eutectic constituent, and solidification temperature range are summarized in Fig. 27. The lines in the bottom two figures represent the fraction eutectic and solidification temperature range, respectively, calculated with the equations above, and there is good agreement between the calculated and measured values. This supports the use of a pseudo binary analog for modeling the solidification behavior of these alloys. More importantly, the results provide a basis for developing a detailed understanding of the weldability results. At low Gd concentrations, the solidification temperature range is high, but the

fraction of terminal eutectic liquid is very low. Thus, the cracking susceptibility is low. As the Gd concentration increases, there is only a slight decrease in the solidification temperature range, but a rather significant increase in the fraction of terminal eutectic liquid. This leads to the increase in cracking susceptibility shown in Fig. 27 that reaches a maximum at ~ 1 wt-% Gd. With still increasing amounts of Gd, the amount of terminal liquid increases to the point where cracking susceptibility decreases due to backfilling of solidification cracks. The reduction in the solidification temperature range with increasing Gd concentration also assists in decreasing the cracking susceptibility. The amount of terminal liquid required to promote backfilling has been suggested to be in the range of 7–10 vol-% (Ref. 48). The results in Fig. 27 support this, where the cracking susceptibility is observed to decrease when the fraction of terminal eutectic reaches this range. This occurs when the Gd concentration reaches ~1.5 wt-%. This phenomenon is also supported by direct observation of backfilling that became appreciable when the Gd reached 1.5 wt-%, as shown in Fig. 25.

These effects can be evaluated in more quantitative detail by combining solidification theory with simple heat flow equations for determining both the size of the crack-susceptible region of the solid + liquid mushy zone and variation in fraction liquid with distance within the mushy re-
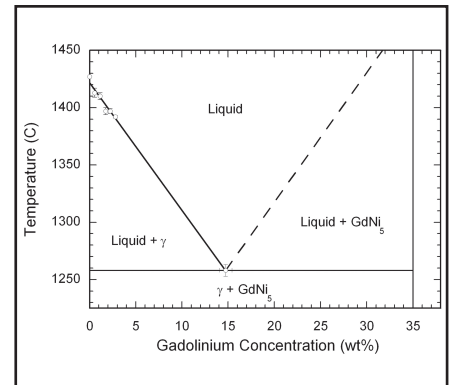
gion. The well-known Scheil equation can also be used to calculate the fraction of liquid (f_L) as a function of temperature via

$$f_L = \left[\frac{T_o - T}{T_o - T_L} \right]^{\frac{1}{k-1}}$$

(5)

where, as before, T_o is the melting point of the Ni-Cr-Mo solvent and T_L is the liquidus temperature of the alloy (as affected by Gd concentration). T is the actual temperature. Noting that k for Gd is 0, Equation 6 reduces simply to

$$f_L = \frac{T_o - T_L}{T_o - T} \quad \text{for } k = 0$$

(6)

The variation in temperature within the solid + liquid region can be estimated using the Rosenthal heat flow solution (Ref. 49) which, for three-dimensional heat flow, is given by

$$T = T_p + \left(\frac{\eta p}{2\pi h r} \right) exp \left[\frac{-S(r-x)}{2\alpha} \right]$$

(7)

where T is the actual temperature, T_p is the preheat temperature, η is the heat source transfer efficiency, P is the arc power, h is the thermal conductivity of the base metal, α is the thermal diffusivity of the base metal, S is the heat source travel speed, r is the radial distance from the heat source, and x is the distance behind the heat source. The weld centerline is of the most interest here because this is the location where the temperature gradient is the lowest and, as a result, where the crack-susceptible solid + liquid region is the largest. This accounts for the experimental observation of the maximum crack length occurring in the weld centerline region. At the weld centerline, r = x and Equation 7 reduces t
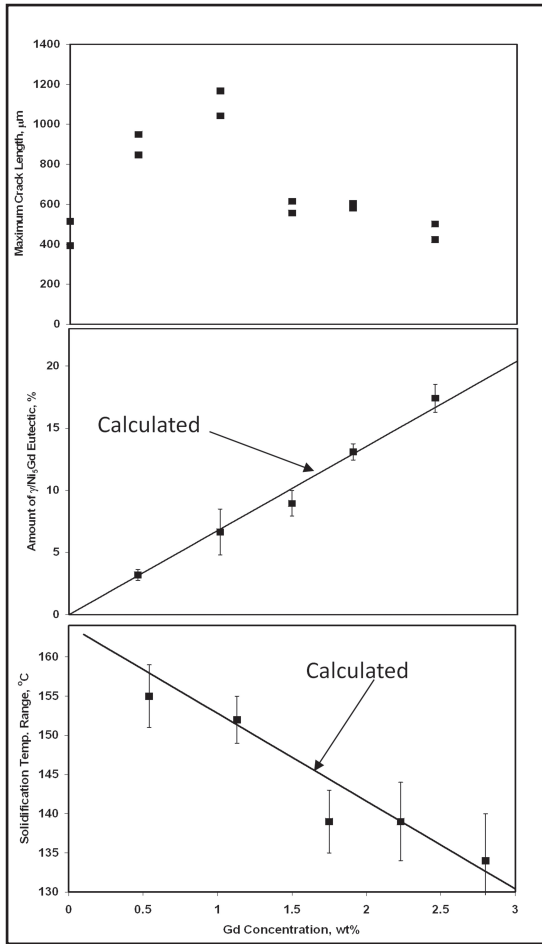
Fig. 27 — Influence of Gd concentration on the cracking susceptibility, amount of terminal eutectic constituent, and solidification temperature range in Alloy C-4.

Fig. 28 — Calculated f_L - x curves for various Gd- containing C-4 alloys.

$$T = T_p + \left(\frac{\eta p}{2\pi hx} \right) \qquad (8)$$

Equation 8 permits an estimate of the temperature variation (T) with position (x) behind the heat source. Thus, these equations can be combined to obtain an expression between the fraction liquid (f_L) and distance along the centerline of the weld x

$$f_L = \frac{-m_l C_o^{Gd}}{T_o - T_p + \frac{\eta p}{2\pi hx}} \qquad (9)$$

This expression is useful because it permits direct estimation of both the variation in fraction liquid with location and the size of the crack-susceptible region of the mushy zone as a function of alloy parameters (T_o, m_L, h, k, C_O^{gd}) and welding parameters (T_o, P). The solid + liquid region will exist where the temperature is between T_L and T_e, and the fraction liquid will vary from 1 at $T = T_L$ to f_e at $T = T_e$.

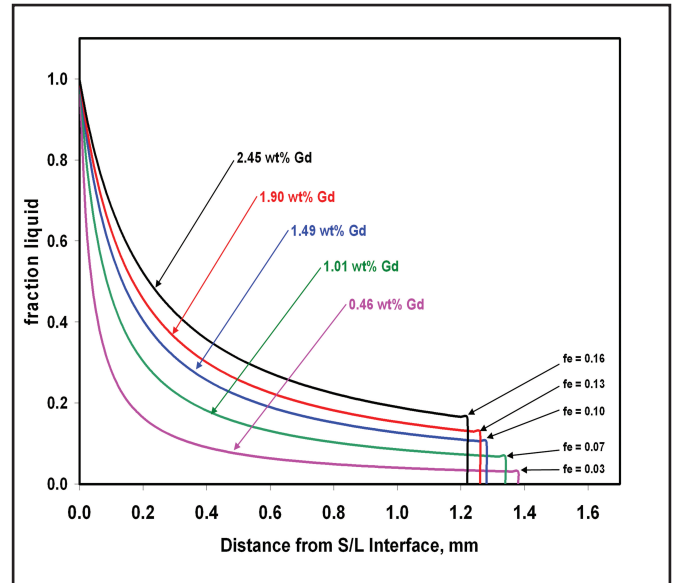Figure 28 shows calculated f_L – x curves for the Gd-containing alloys evaluated here. The curves have all been shifted so that the reference point is taken as distance from the solid/liquid interface where $f_L = 1$ (instead of distance from the heat source). This shift permits more direct comparison between curves of different nominal Gd concentrations. The terminal fraction eutectic values (f_e) calculated to form at the edge of the mushy zone for each alloy are also noted in the figure.

It should be noted that the variation in temperature with position calculated through Equation 8 is not expected to be highly accurate due to the assumptions invoked to arrive at the Rosenthal solution, most notably that the thermal properties are assumed constant with temperature and the heat flow via convection in the melt pool is ignored. However, the objective here is to evaluate the influence of nominal composition on the solid + liquid zone characteristics and resultant weldability under identical heat flow conditions. In view of this, it is only required to have an estimate of the functional form of the temperature variation with the mushy zone. As demonstrated by the good comparison between experimental and calculated values of ∆T and f_e, the influence of nominal composition on mushy zone characteristics can be accurately captured with these equations. This is also confirmed by noting that the experimentally determined maximum crack lengths shown in Fig. 24 and the calculated mushy zone sizes shown in Fig. 28 are of similar size. Solidification cracks are not expected to propagate through the high temperature region of the mushy zone where the liquid fraction is high because solid-solid boundaries have not yet begun to form in these regions, but rather are constrained to a region within the mushy zone. Thus, the maximum crack length values should be less than the size of the mushy region, and this trend is certainly observed by the maximum crack lengths shown in Fig. 27 and the mushy zone sizes shown in Fig. 28.

More importantly, the calculated f_L – x curves, combined with the experimental weldability results, aid in the development of a more detailed understanding on the influence of Gd on the mushy zone characteristics and resultant cracking susceptibility. At the lowest Gd concentration (0.46 wt-%), the mushy zone is the largest because the solidification temperature range is the widest. In addition, much of the mushy zone is occupied by relatively low f_L values. For example, the fraction liquid only varies from 0.03 at the edge of the mushy zone (at x ≈ 1.4 mm) to 0.07 at a distance of 0.5 mm behind the solid/liquid interface, (i.e., ~ 65% of the mushy zone is occupied by 0.03 < f_L < 0.07). This liquid fraction range is high enough to cause moderate cracking, but too low for appreciable backfilling and healing of the cracks. The mushy zone size for the 1.01 wt-% Gd alloy is slightly reduced due to the smaller solidification temperature range. However, the higher amount of liquid present in the trailing edge of the mushy zone aggravates cracking by preventing the formation of solid/solid boundaries, and the terminal fraction liquid value of 0.07 is too low to permit healing of cracks by backfilling. This suggests that, at a terminal value of fe ≈ 0.07 and below, the liquid from the molten pool is cutoff from cracks that form in the mushy zone because the solid dendritic morphology is well developed.

At Gd concentrations of 1.49 wt-% and higher, the f_L values never drop below 0.10 in the mushy zone. Also note that the f_L values do not decrease as substantially with increasing distance for these higher Gd alloys. Each of these factors would help promote a more continuous liquid phase between the fully molten weld pool and the solid + liquid mushy zone, thus permitting the backfilling that was observed experimentally. The decrease in solidification temperature range that occurs due to a reduction in the liquidus temperature also contributes to the improved cracking susceptibility of the alloys with Gd concentration higher than 1.49 wt-%.

Summary

The ever-increasing demand to produce energy from a variety of ever-decreasing resources has created the need to develop new plants that use existing fuel sources more efficiently. This, in turn, places a heavy demand on developing new engineering alloys that can be utilized in aggressive conditions that cannot be tolerated by existing alloy systems. As the alloys become more complex, it is likely that they will also be subjected to more complicated changes in microstructure during the weld thermal cycle. In view of this, it is important for alloy producers, end users, and research organizations to collaborate so that welding technology can be developed in parallel with the discovery of new materials. This approach will permit strategic changes to new alloys during the design stage, thus avoiding the potential for limited use of newly developed alloys in applications where welding is required.

It is important to note that many of the inferior properties of fusion welds are related to the steep gradients in chemical composition and microstructure that form across the heat-affected zone and fusion zone. Thus, emphasis in future research should be placed on understanding, controlling, and where required, minimizing these gradients through alloy and process control. Computational modeling can play a key role in this area by accelerating the understanding of microstructure and property changes that occur during welding. While significant progress is being made on the front of microstructural modeling, much work is still needed to predict mechanical properties of welds from knowledge of the microstructure. Similarly, techniques are needed to determine long-term creep properties from short-term tests. This area is particularly challenging because the long-term creep properties are invariably controlled by microstructural changes that occur at very long times, and these changes can be difficult to properly simulate with short-term tests.

Lastly, training of graduate-level engineers is also vitally important to ensure safe and reliable operation of welded structures that will be used in energy applications. While physical metallurgy forms the basic discipline for understanding the complex phase transformations that occur during welding, the number of engineers with basic skills in physical metallurgy has declined over the years as this form of training gets replaced with other "modern" materials topics in areas such as nanotechnology, biotechnology, etc. While these fields are certainly important, it is equally important to ensure a sufficient level of graduate engineers are trained to meet the demands of industrial fabrication and maintenance required in energy and other areas that rely so heavily on manufacturing. Industry can play an important role in this area through support of graduate research programs in order to fill the gap from government funding that has declined over the years. A successful example of industry/university collaboration is currently represented by the National Science Foundation Center on Integrated Materials Joining Science for Energy Applications. This center is a joint effort through four universities (Ohio State, Lehigh, Colorado School of Mines, and University of Wisconsin-Madison) that is supported by both NSF and 31 member companies. Research at the center is focused on a wide range of issues related to joining for energy applications while simultaneously supporting $\sim$ 30 graduate students who are often hired by member companies. This type of industry/university collaboration is essential for continuing to meet the future needs of welding and metallurgical engineers.

References

1. Annual Energy Review. 2011. U.S. Energy Information Administration, DOE/EIA-Report 0384.
2. International Energy Outlook. 2013. DOE.EIA Report 0484.
3. Pauling, L. 1938. The nature of the interatomic forces in metals. *Physical Review* 54: 899–904.
4. Jones, C. 1997. *Power* January/February, pp. 54–60.
5. Whitaker, R. 1982. *EPRI Journal* pp. 18–25.
6. Urich, J. A., and Kramer, E. 1996. *FACT* American Society of Mechanical Engineers, 21: 25–29.
7. Kung, S. C., and Bakker, W. T. 1997. *Mater. High Temp.* 14: 175–182.
8. Deacon, R. M., DuPont, J. N., and Marder, A. R. 2007. *Materials Science & Engineering* A, 460-461: 392–402.
9. Luer, K .R., DuPont, J. N., Marder, A. R., and Skelonis, C. K. 2001. Corrosion fatigue of Alloy 625 weld claddings exposed to combustion environments. *Materials at High Temperatures*, 18: 11–19.
10. Dooley, R. B., and Chang, P. 1997. The current status of boiler tube failures in fossil plants. *International Conference on Boiler Tube Failures in Fossil Plants,* EPRI, Nashville, Tenn.
11. DuPont, J. N., Stockdale, A. W., Caizza, A., and Esposito, A. 2013. High temperature corrosion behavior of Alloy 600 and 622 weld cladding and coextruded coatings. *Welding Journal* 92(7): 218-s.
12. DuPont (primary author), J. N., Lippold, J. C., and Kiser, S. D. 2009. *Welding Metallurgy and Weldability of Nickel Base Alloys*, John Wiley & Sons, Hoboken, N.J.
13. Lai, G. Y. 2007. *High Temperature Corrosion and Materials Applications.* ASM International, Materials Park, Ohio.
14. Nied, H. F. 1987. Periodic array of cracks in a half-plane subjected to arbitrary loading. *Journal of Applied Mechanics* 109: 642–648.
15. Benthem, J. P., and Koiter, W. T. 1973. Asymptotic approximations to crack problems. G. C. Sih ed. *Methods of Analysis and Solutions of Crack Problems*. Noordhoff, Netherlands, pp. 131–178.
16. Regina, J. R., DuPont, J. N., Marder, A. R. 2004. Corrosion behavior of Fe-Al-Cr alloys in sulfur- and oxygen-rich environments in the presence of pyrite. *Corrosion*, Houston, Tex., 60(5): 501–509.
17. Regina, J. R., DuPont, J. N., and Marder, A. R. 2005. Gaseous corrosion resistance of Fe-Al-based alloys containing Cr additions Part I: Kinetic results. *Mater Sci Eng*, A, A404(1-2): 71–78.
18. Viswanathan, R. 2003. Boiler materials for USC plants. DOE-NETL Presentation. *www.netl.doe.gov/publications/proceedings/03/materials/Viswanathan.pdf*.
19. Patel, S. J., deBarbadillo, J. J., Baker, B. A., and Gollihue, R. D. 2013. Nickel base superalloys for next generation coal fired AUSC power plants. *Procedia Engineering, 6th International Conference on Creep, Fatigue and Creep-Fatigue Interaction*, 55: 246–252.
20. Bechetti, D. H., DuPont, J. N., deBarbadillo, J. J., and Baker, B. A. 2013. Homogenization and dissolution kinetics of fusion welds in INCONEL® Alloy 740H. Accepted for publication in *Metallurgical and Materials Transactions*.
21. Bechetti, D. H., and DuPont, J. N. 2013. Microstructural evolution of IN740 fusion welds during creep rupture. Manuscript in preparation for submission to *Metallurgical and Materials Transactions*.
22. Kloc, L. 1996. On the symmetry of denuded zones in diffusional creep. *Scripta Materialia* 35: 539–541.
23. Cao, W. D., and Kennedy, R. L. 2001.

Thermal stability of Alloys 718 and Allvac 718-ER (Ref. registered trademark). *SUPERAL-LOYS 718, 625, 706 and Various Derivatives*, pp. 455–464.

24. Baither, D., Herding, T., Krol, T., Reichelt, R., and Nembach, E. 2001. The effects of precipitation free zones on order strengthening in NIMONIC PE16 bi-crystals. *Materials Science and Engineering* A 319-321: 279–283.

25. Krol, T., Baither, D., and Nembach, E. Quantification of the detrimental effects of precipitate free zones on the yield strength of a superalloy. *Scripta Materialia* 48: 1189–1194.

26. Krol, T., Baither, D., and Nembach, E. 2004. Softening of the superalloy NIMONIC PE16 by precipitate free zones along grain boundaries. *Materials Science and Engineering* A 387-389: 214–217.

27. Baither, D., Krol, T., and Nembach, E. Dislocation processes in precipitate-free zones in NIMONIC PE16 studied by in-situ transmission electron microscopy. *Materials Science and Engineering* A 387-389: 163–166.

28. Wu, X.-J., and Koul, A. K. 1995. Grain boundary sliding in the presence of grain boundary precipitates during transient creep. *Metallurgical and Materials Transactions* A: *Physical Metallurgy and Materials Science* 26 A, pp. 905–914.

29. Baither, D., Krol, T., and Nembach, E. 2003. In-situ transmission electron microscopy study of dislocation processes at precipitate-free zones in a -strengthened superalloy. *Philosophical Magazine* 83: 4011–4029.

30. Maldonado, R., and Nembach, E. 2007. Formation of precipitate free zones and the growth of grain boundary carbides in the nickel-base superalloy NIMONIC PE16. *Acta Materialia* 45: 213–224.

31. Qin, X. Z., Guo, J. T., Yuan, C., Chen, C. L., and Ye, H. Q. 2007. Effects of long-term thermal exposure on the microstructure and properties of a cast Ni-base superalloy. *Special Section: Symposium on Dynamic Behavior of Materials (Part II)* 38 A, 3014–3022.

32. Wadsworth, J., Ruano, O. A., and Sherby, O. D. 2002. Denuded zones, diffusional creep, and grain boundary sliding. 33: 219–229.

33. McNee, K. R., Greenwood, G. W., and Jones, H. 2002. The effect of stress orientation on the formation of precipitate free zones during low stress creep. *Scripta Materialia* 46: 437–439.

34. Tien, J. K., Gamble, R. P. 1971. *Influence of Applied Stress and Stress Sense on Grain Boundary Precipitate Morphology in a Nickel-Base Superalloy During Creep* 2, 1663–1667.

35. Zener, C. 1949. *Journal of Applied Physics*, 20: 950–959.

36. Hull, L., Pace, M., Lessing, P., Rogers, R., Mizia, R., Propp, A., Shaber, E., and Taylor, L. 2000. *Advanced Neutron Absorbers for DOE SNF Standardized Canisters — Feasibility Study,* Idaho National Engineering and Environmental Laboratory Report DOE/SNF/REP-057 Rev. 0.

37. DuPont, J. N., Robino, C. V., Michael, J. R., Mizia, R. E., and Williams, D. B. 2004. Physical and welding metallurgy of Gd-enriched tions — Part II: Nickel base alloys. *Welding Journal* 83(11): 289-s to 300-s.

38. Susan, D. F., Robino, C. V., Minicozzi, M. J., and DuPont, J. N. 2006. A solidification diagram for Ni-Cr-Mo-Gd alloys estimated by quantitative microstructural characterization and thermal analysis. *Metallurgical and Materials Transactions*, Vol. 37A, pp. 2817–2825.

39. Van Konynenburg, R. A., Curtis, P. G., Summers, T. S. E. 1998. Scoping corrosion tests on candidate waste package basket materials for the Yucca Mountain project. Report UCRL-ID-130386, Lawrence Livermore National Laboratory.

40. Mizia, R. E., Robino, C. V., and DuPont, J. N. 2006. Development and testing of an advanced neutron absorbing gadolinium alloy for spent fuel storage. *Nuclear Technology*, Vol. 155, August.

41. DuPont, J. N., and Marder, A. R. 1996. Dilution in single pass arc welds. *Metallurgical and Material Transactions* B, Vol. 27B, pp. 481–489.

42. Cieslak, M. J. 1991. The welding and solidification metallurgy of Alloy 625. *Welding Journal* 70(2): 49-s to 56-s.

43. DuPont, J. N., Robino, C. V., and Marder, A. R. 1998. Solidification and weldability of Nb-bearing superalloys. *Welding Journal* 77(10): 417-s to 431-s.

44. *Binary Alloy Phase Diagrams*. 1992. Vol. 3, ASM International, Materials Park, Ohio.

45. Scheil, E. 1942. *Z. Metallk*. 34: 70.

46. David, S. A., and Vitek, J. M. 1989. *International Materials Review*. 34: 213–245.

47. Kou, S. 2003. *Welding Metallurgy*, 2nd Edition, pp. 170–172, John Wiley & Sons, Hoboken, N.J.

48. Clyne, T. W., and Kurz, W. 1982. The effect of melt composition on solidification cracking of steel, with particular reference to continuous casting. *Metall. Trans.* B, Vol. 13A, pp. 259–266.

49. Rosenthal, D. 1941. *Welding Journal* 20(5):220-s.